

# MEMS Nanopositioner for On-Chip Atomic Force Microscopy: A Serial Kinematic Design

Mohammad Maroufi, *Student Member, IEEE*, Anthony G. Fowler, *Member, IEEE*,  
and S. O. Reza Moheimani, *Fellow, IEEE*

**Abstract**—The design and characterization of a two-degree-of-freedom serial kinematic microelectromechanical systems (MEMS) nanopositioner for on-chip atomic force microscopy (AFM) is reported. A novel design is introduced to achieve a serial kinematic mechanism based on a standard silicon-on-insulator MEMS fabrication process. The nanopositioner comprises a slow axis with a resonance frequency of 2.4 kHz and a fast axis with a resonance frequency of above 4.4 kHz, making it ideal for rastering, as required in the AFM. Strokes of 14 and 9  $\mu\text{m}$  are experimentally achieved for the fast and slow axes, respectively. The serial kinematic design of the stage enables the cross-coupling between the two axes of motion to be as low as  $-60$  dB. Electrothermal displacement sensors are incorporated in the device, which may be used to enable feedback control as required in high-speed AFM. [2014-0248]

**Index Terms**—Nanopositioner, MEMS, atomic force microscopy, serial kinematic mechanism.

## I. INTRODUCTION

NANOPOSITIONING stages are used as an integral component in numerous scientific and technological applications. These devices can provide high-precision, repeatable motion with nanometer or sub-nanometer resolution. The growing need for precise positioning, manipulation, and interrogation of matter in the micro to nanoscale range is a significant driver for developing fast and highly-accurate nanopositioners [1], [2]. Nanopositioners are also extensively used in various forms of scanning probe microscopy (SPM), particularly in the atomic force microscope (AFM) [2].

In an AFM, a sample's topography can be obtained by scanning the entire sample in a particular trajectory using a probe, which features a cantilever with a very sharp tip. A 3D image of the sample can be produced based on the cantilever tip deflection and the nanopositioner's lateral position data [3], [4]. Hence, the image resolution obtained by the AFM is a strong function of the positioning precision

of the probe relative to the sample, which is the task performed by the nanopositioner. In addition, the bandwidth of the nanopositioner determines the highest possible scanning speed. High-bandwidth nanopositioning is a critical enabling technology for high-speed AFMs currently under development. Equipped with high-bandwidth nanopositioners, state-of-the-art AFMs are able to produce real-time images of micro and/or nanoscale substances and processes with fast dynamics, such as the interaction of biomolecules [2], [5].

The majority of nanopositioners proposed in the literature for AFM, including piezoelectric tubes and different types of flexure-guided nanopositioners, are macro-sized devices [2], [6]. However, recent efforts to build a single-chip AFM have led to the emergence of a number of micro-sized nanopositioners realized through microelectromechanical systems (MEMS) fabrication processes [4], [7]–[9]. In addition to a small form factor, MEMS nanopositioners are potentially able to offer a variety of advantages over their macro-sized counterparts such as batch fabrication capability and a higher achievable bandwidth, mainly due to the adoption of silicon as the structural material [10].

From a design perspective, nanopositioners can be designed based on either the serial kinematic mechanism (SKM) or the parallel kinematic mechanism (PKM). An SKM can be realized by stacking one kinematic chain within another, while in a PKM, both kinematic chains are connected directly to the scanner table. Almost all MEMS nanopositioners reported in the literature for AFM applications follow a parallel kinematic design [4], [7], [8], [10]. This design approach, however, is known to lead to certain drawbacks. For example, the cross-coupling between the two axes of motion can be significant, resulting in artifacts in the generated AFM image. Furthermore, the two axes are typically designed to have identical bandwidths, while for rastering applications only one high-bandwidth axis is needed [2], [11].

Alternatively, an SKM is highly suitable for MEMS nanopositioning for AFM applications [5]. A MEMS SKM scanner can be designed to achieve a high bandwidth over one axis with minimal cross-coupling to the orthogonal slow axis, which is a requirement for fast and distortion-free AFM imaging. Although SKM designs have been successfully implemented in macro-sized nanopositioners, their implementation in MEMS requires overcoming challenges such as signal routing to the inner stage [2], [12].

There are a limited number of MEMS nanopositioners reported in the literature based on serial kinematic design

Manuscript received August 15, 2014; revised April 10, 2015; accepted May 2, 2015. Date of publication June 1, 2015; date of current version November 25, 2015. This work was supported in part by the Australian Research Council and in part by the University of Newcastle, Callaghan, NSW, Australia. Subject Editor M. Wong.

M. Maroufi and A. G. Fowler are with the School of Electrical Engineering and Computer Science, University of Newcastle, Callaghan, NSW 2308, Australia (e-mail: mohammad.maroufi@uon.edu.au; anthony.fowler@uon.edu.au).

S. O. Reza Moheimani is with the Department of Mechanical Engineering, University of Texas at Dallas, Richardson, TX 75080 USA (e-mail: reza.moheimani@utdallas.edu).

Color versions of one or more of the figures in this paper are available online at <http://ieeexplore.ieee.org>.

Digital Object Identifier 10.1109/JMEMS.2015.2434390

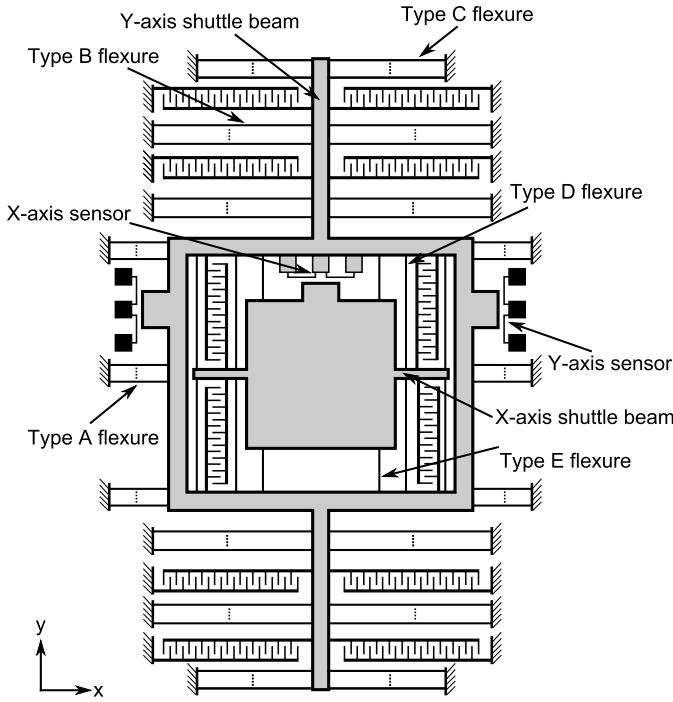


Fig. 1. The schematic design of the proposed serial kinematic MEMS nanopositioner.

for optical MEMS and manipulation applications [13], [14]. In these examples, the signal routing problem was addressed by using the electrical isolation provided by the buried oxide layer in silicon-on-insulator (SOI) wafers. However, neither nanopositioner features on-chip displacement sensors, and instead utilize a bulky optical displacement sensing mechanism. In addition, both nanopositioners demonstrate a relatively low bandwidth. Considering these drawbacks, none of these designs is suitable for implementation in high-speed on-chip AFMs.

In this paper, we report a serial kinematic MEMS nanopositioner realized through a standard SOI-MEMS fabrication process. The issue of signal routing to the inner stage is addressed by exploiting the electrical insulating property of the buried oxide layer on a suspended substrate structure. To make it possible for the nanopositioner to be used in an AFM, electrothermal displacement sensors are implemented in each direction. The feasibility of implementing a capacitive displacement sensing technique for the inner stage is also investigated. The proposed nanopositioner demonstrates high bandwidth in one axis of motion and negligible cross-coupling to the orthogonal slow axis, making it highly suitable for use in a high-speed on-chip AFM.

## II. NANOPositionER MECHANICAL DESIGN AND FABRICATION

### A. Design

The nanopositioning stage is designed as an SKM [2]. To move the scan table in two orthogonal directions, two independent kinematic chains are designed so that one is embedded within the other. A schematic of the nanopositioner is provided in Fig. 1. The scan table has dimensions  $1.7 \text{ mm} \times 1.7 \text{ mm}$

TABLE I  
GEOMETRICAL PROPERTIES OF THE NANOPositionER

		Length ( $\mu\text{m}$ )	Width ( $\mu\text{m}$ )	Number
Flexure Type	A	650	7	88
	B	1800	8	32
	C	1287	6	20
	D	1310	15	8
	E	520	12	4
Comb Fingers	Gap: $2\text{ }\mu\text{m}$ , Engagement: $9\text{ }\mu\text{m}$ Length: $22\text{ }\mu\text{m}$ , Width: $2\text{ }\mu\text{m}$			
Frame	Size: $3500\text{ }\mu\text{m} \times 3140\text{ }\mu\text{m}$ , Width: $200\text{ }\mu\text{m}$			
Inner Combs	Small	Length: $500\text{ }\mu\text{m}$ , Number per side: 16		
	Large	Length: $1280\text{ }\mu\text{m}$ , Number per side: 8		
Outer Combs	Length: $1770\text{ }\mu\text{m}$ , Number per side: 14			
Total Size	$4.8\text{ mm} \times 7.08\text{ mm}$			

and is located at the centre of the inner stage. The inner stage comprises two sets of electrostatic comb drives which are connected to the scan table via shuttle beams on both sides. The electrostatic actuators move the scan table in the X direction, while straight beams (denoted as ‘type D’ and ‘E’) are used as the suspension system.

The entire inner kinematic chain and the scan table are positioned within a rectangular shaped frame as shown in Fig. 1. The frame is suspended by ‘type A’ flexures and is connected on both sides to the Y direction shuttle beams. These shuttle beams connect the electrostatic actuators and other suspension flexures (‘type B’ and ‘C’) to the frame. The geometrical properties of the device are reported in Table I.

As illustrated in Fig. 1, straight beam electrothermal sensors [15] are implemented in the design to measure the stage displacement in both axes. The inner sensor is located on the suspended frame and is used to measure the X direction displacement via the heat sink integrated with the scan table. The outer electrothermal sensors are placed so that they measure the frame displacement in the Y direction.

### B. Fabrication and Working Principle

Scanning electron microscope (SEM) images of the fabricated stage are shown in Fig. 3. The fabrication process was performed using MEMSCAP’s standard SOIMUMPs process [16]. The SOI wafer in this fabrication process comprises a handle layer (substrate) with a thickness of  $400 \mu\text{m}$ , a  $2 \mu\text{m}$ -thick buried oxide layer on the substrate, and a top doped single crystal silicon layer with a thickness of  $25 \mu\text{m}$  used as the device layer.

The fabrication process steps are schematically illustrated in Fig. 2. Initially a metal layer comprising  $20 \text{ nm}$  of chrome and  $500 \text{ nm}$  of gold is deposited and patterned to implement electrical connections. Then, deep reactive ion etching (DRIE) is used to pattern the device layer. Using reactive ion etching (RIE) and subsequently DRIE from the back side of the wafer, the substrate is patterned. The oxide layer halts both the DRIE and RIE etching processes. This layer beneath the suspended silicon structure is removed, and consequently the suspended mechanical structure is released.

Due to the doping of the device layer, all mechanically connected structures fabricated using this layer are also

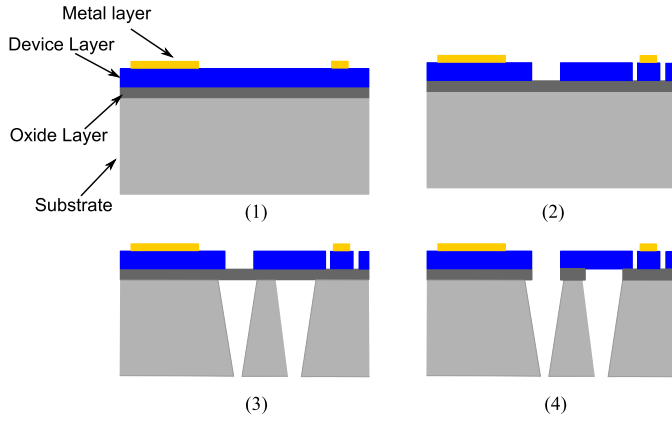


Fig. 2. Schematic of the fabrication process sequence. (1) Metal layer deposition. (2) DRIE of the device layer. (3) Patterning of the substrate using RIE and DRIE. (4) Oxide layer etching and releasing.

electrically connected. Hence, all mechanical structures made from the device layer are electrically equipotential, which makes it difficult to provide the electrical actuation and sensing signals for the inner stage. To overcome this problem while maintaining the mechanical integrity of the device, sections of the substrate are suspended, as shown in the underside view in Fig. 3. Here, the substrate is not etched underneath the upper and lower edges of the frame. The presence of the insulating buried silicon oxide layer on the suspended substrate allows the mechanical components micro-machined out of the structural silicon layer to remain mechanically connected, but electrically isolated. This method makes the creation of electrical paths to the inner stage components possible.

In Fig. 4, a schematic of the signal routing paths in the proposed design is shown. For the sake of clarity, each signal path is denoted by a different color. To provide the actuation signal for the inner stage, some of the ‘type A’ flexures on each side are used. The signal is routed using part of the frame to all electrostatic actuators in the inner stage.

As will be explained in more detail in Sec. II-D, three electrical connections are needed for each electrothermal sensor. To route electrical signals to the sensor in the inner stage, ‘type A’ flexures are also used on both sides of the frame as indicated by blue in Fig. 4. The third electrode (the common electrode) of the inner sensor is connected to the electrical ground using the Y-axis shuttle beam. To decrease the resistance of the signal path for the electrothermal sensor in the inner stage, a metal layer with a width of  $3\ \mu\text{m}$  is deposited on four of each of the ‘type A’ and ‘type B’ flexures. To make the deposition of the metal layer on top of these flexures possible given the fabrication process constraints, the width of these flexures was chosen to be  $9\ \mu\text{m}$ .

### C. Mechanical Modeling

As mentioned earlier, straight beams are used as the suspension in the mechanical design. As shown in Fig. 5, these beams are rigidly fixed at one end, and due to their symmetrical position with respect to the shuttle beams, have a guided support or slider constraint applied at the other end.

Using Euler-Bernoulli beam theory under small deflection conditions, the deflection of the beam in the presence of an external force ( $F_{ext}$ ) is:

$$\delta = F_{ext}L^3/(12EI) \quad (1)$$

where  $I$  is the moment of inertia of the beam’s cross section, and  $E$  is the Young’s Modulus of the structural material. Since the deflection equation of the beam in both the transverse and out-of-plane directions has the same boundary conditions, by calculating  $I$  for each bending condition, the stiffness in both directions can be obtained as follows:

$$\begin{aligned} I_t &= \frac{hw^3}{12} K_t = \frac{Ehw^3}{L^3} \\ &\quad \& \\ I_z &= \frac{h^3w}{12} K_z = \frac{Eh^3w}{L^3}. \end{aligned} \quad (2)$$

In (2),  $K_t$  and  $K_z$  are the transverse and out-of-plane stiffness, respectively. The stiffness obtained by (2) was used to approximate the first resonant frequency of the device in the in-plane and out-of-plane directions using a lumped parameter modeling approach (3),

$$f = \frac{1}{2\pi} \sqrt{\frac{K}{M + \sum m_{eq}}} \quad (3)$$

where  $M$  is the total mass connected to the suspension beam and  $K$  is the total stiffness in the direction of motion.  $m_{eq}$  is the mass contribution of each suspension beam in the first in-plane resonant mode of the stage. This contributed mass for each beam was estimated based on their static deflection as a fraction of their total mass ( $m_{beam}$ ) and represented as a lumped parameter as follows [7]:

$$m_{eq} = \frac{13}{35} m_{beam}. \quad (4)$$

To make the device robust and more conducive to controller implementation, as a design criterion, the first two resonant modes of the system should occur in the X and Y directions [17] while other out-of-plane modes are designed to be at higher frequencies. This condition was satisfied by tuning the suspension beams’ width and their total number in order to increase the Z-axis stiffness while leaving the in-plane stiffness relatively unchanged.

The displacement achievable by the stage is another design parameter considered here. The force generated by the comb drives with an actuation voltage of  $V$ , and the resulting displacement of the stage ( $\delta_t$ ) can be obtained by (5).

$$F_e = \frac{n\epsilon_0 h}{g} V^2 \Rightarrow \delta_t = \frac{n\epsilon_0 h}{Kg} V^2 \quad (5)$$

In (5),  $\epsilon_0$  is the permittivity of the air, and  $n$  and  $g$  are the number of comb finger pairs and the air gap between each comb, respectively. Note that due to the fabrication process properties, the thickness ( $h$ ) of the suspension system and the comb fingers are equal. The comb structures are designed to transfer the generated force from the comb fingers to the shuttle beams in each axis. To reduce the mass of the comb structures, and as a result increase the achievable

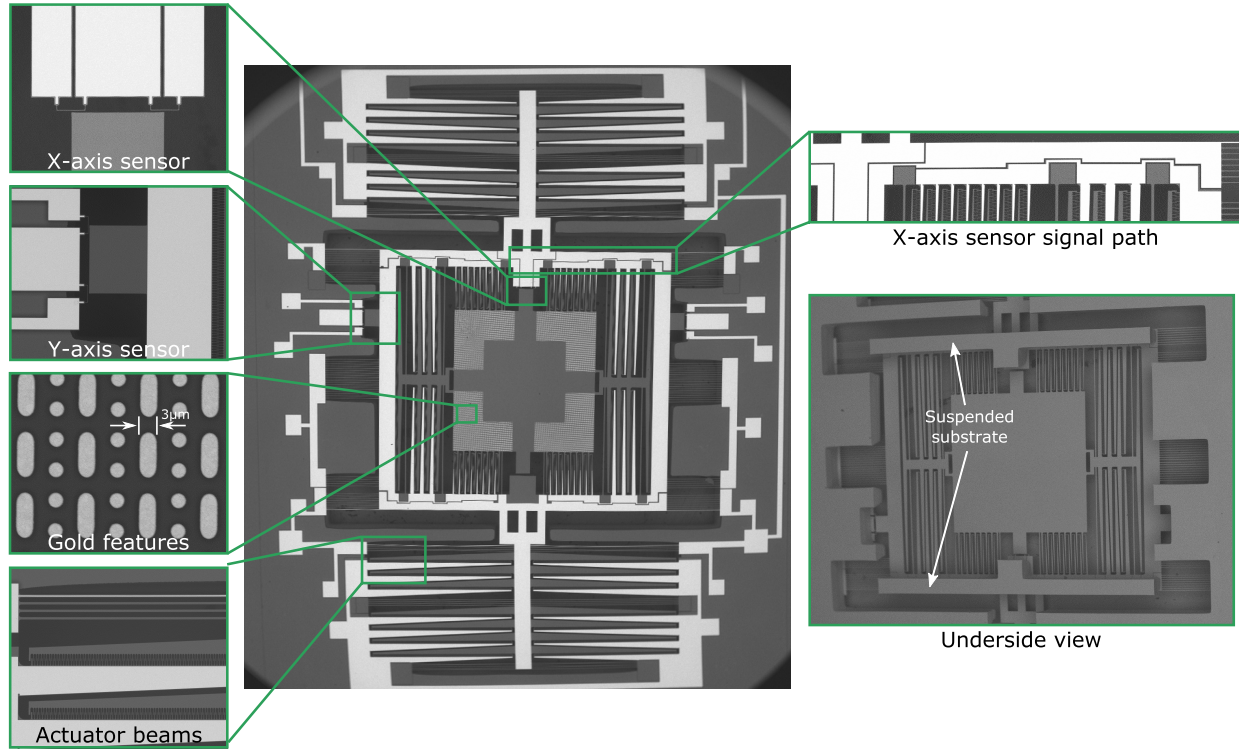


Fig. 3. SEM images of the fabricated nanopositioner. The bright areas in the image is the deposited gold layer, while the underside view shows the suspended substrate beneath the frame.

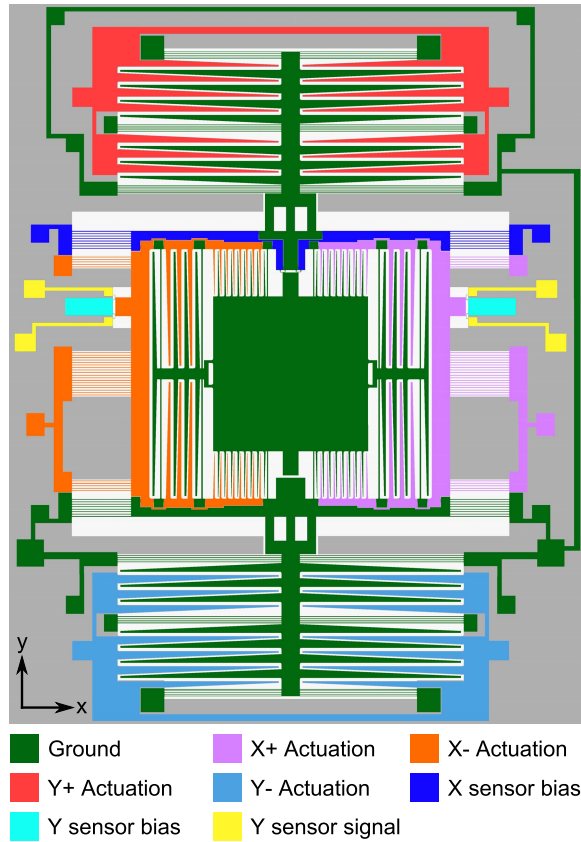


Fig. 4. The signal paths of the serial kinematic stage.

resonance frequency, the comb structures are designed to have a trapezoidal shape in both axes. Their in-plane deflection under the presence of a distributed electrical force obtained

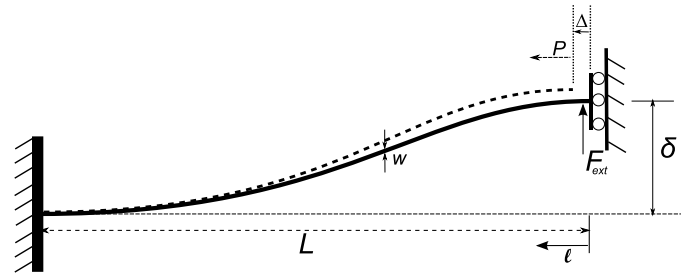


Fig. 5. The in-plane deflection of the suspension beam under the influence of external force  $F_{ext}$ . The deflection of the beam ( $\Delta$ ) due to force  $P$  is used to calculate the stiffness of the beam in the  $l$  direction.

by (5) was examined using a finite element model (FEM) to be in an acceptable range.

For both axes, having comb drives incorporated on both sides of the stage allows the quadratic nonlinearity in the electrostatic force-voltage characteristic of the comb drives (refer to (5)) to be mitigated by applying a linear actuation method [7]. In this mechanism, a differential actuation voltage ( $v_{ac}$ ) plus a DC voltage bias ( $V_{dc}$ ) are applied to the stator combs while the rotor combs are electrically grounded (represented by the green color in Fig. 4). The total force exerted on the stage using this actuation mechanism is presented in (6). It is clear that the net force has a linear relationship with  $v_{ac}$ .

$$F_{net} = \frac{n\epsilon_0 h}{g} [(V_{dc} + v_{ac})^2 - (V_{dc} - v_{ac})^2] = \frac{4n\epsilon_0 h}{g} V_{dc} v_{ac} \quad (6)$$

1) *Lateral Instability Avoidance*: Lateral instability (also known as ‘snap-in’) happens when the moving and stationary

combs are pulled together in the lateral direction (with respect to the direction of motion) and stick together, which results in an electrical short that may cause damage to the comb drive structures. To develop a design condition based on which this lateral instability can be avoided, the electrical stiffness ( $K_e$ ) [18] is defined in (7),

$$K_e = \frac{2n\epsilon_0 h(d + d_0)}{g^3} V^2 \quad (7)$$

where  $d$  and  $d_0$  are the displacement and initial engagement of the comb fingers, respectively. The electrical stiffness defined in (7) can be considered as a ‘negative’ stiffness; if the moving comb fingers were to be displaced from their original position, the net electrostatic force pushes them further away rather than pulling them back to the equilibrium position. To prevent lateral instability, the longitudinal stiffness provided by the mechanical suspension system should be larger than the electrical stiffness.

The longitudinal stiffness ( $K_s$ ) of the clamped-guided beam obtained by Hooke’s Law is:

$$K_s = \frac{Ehw}{L}. \quad (8)$$

However, (8) is only valid when the beam does not experience any transverse deflection. To obtain the longitudinal stiffness of the beam while it encounters a transverse deflection of  $\delta$ , the Rayleigh-Ritz method can be used. In this method, an admissible trial function should be initially proposed for the beam deflection satisfying the boundary conditions. Then, the deflection of the beam ( $\Delta$  in Fig. 5) can be obtained in the presence of the force  $P$  by extremization of the total potential energy [18], [19]. Using this method, the deflection of the beam in the  $l$  direction is:

$$\Delta = \frac{3PL\delta^2}{25EI_l}. \quad (9)$$

Considering (9), the deflection-dependent stiffness ( $K_p$ ) can be calculated for the longitudinal direction as:

$$K_p = \frac{25EI_l}{3L\delta^2}. \quad (10)$$

Using  $K_p$ , the actual longitudinal spring constant of the clamped-guided beam ( $K_l$ ) is the series connection of two springs (8) and (10) which can be obtained as [18]:

$$K_l = (K_p^{-1} + K_s^{-1})^{-1}. \quad (11)$$

In Fig. 6, the variation of the longitudinal stiffness with displacement is shown. The total stiffness ( $K_l$ ) is normalized with respect to the stiffness obtained by Hooke’s Law ( $K_s$ ). It is clear that the longitudinal stiffness shows a softening behavior with increasing transverse deflection. In addition, (7) shows that the ‘negative’ electrical stiffness ( $K_e$ ) is increasing with the displacement of the stage. Therefore, to avoid snap-in occurring, the total longitudinal stiffness provided by the mechanical suspension system should be larger than  $K_e$  with an acceptable margin at the maximum intended transverse displacement.

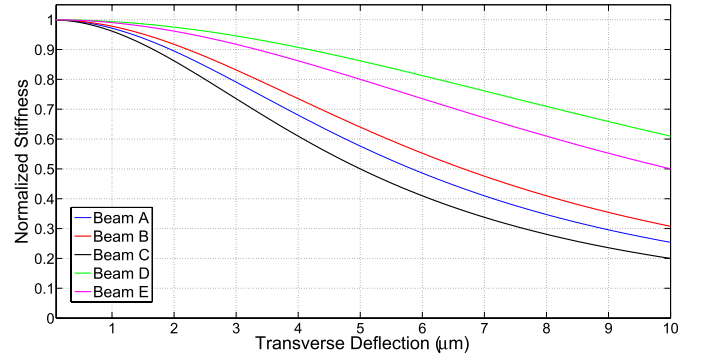


Fig. 6. The normalized longitudinal stiffness ( $K_l/K_s$ ) variation versus displacement, obtained for all beam types in the design.

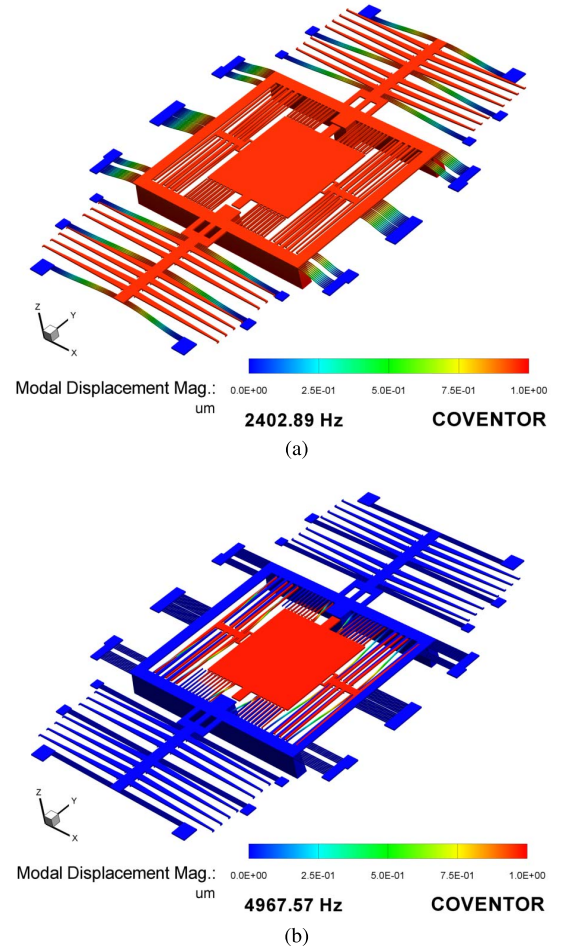


Fig. 7. Finite element modal analysis results, showing (a) the first resonant mode along the Y direction and (b) the second resonant mode along the X direction.

2) *Finite Element Model*: After obtaining initial dimensions from the theoretical model, an FEM was also constructed using CoventorWare MEMS design software. As illustrated in Fig. 7, the modal analysis reveals that the first and second resonant modes are in-plane along the Y and X axes, and are located at approximately 2.4 kHz and 5 kHz, respectively. As expected, the combined mass of the inner stage and the suspended substrate sections lowers the resonance frequency



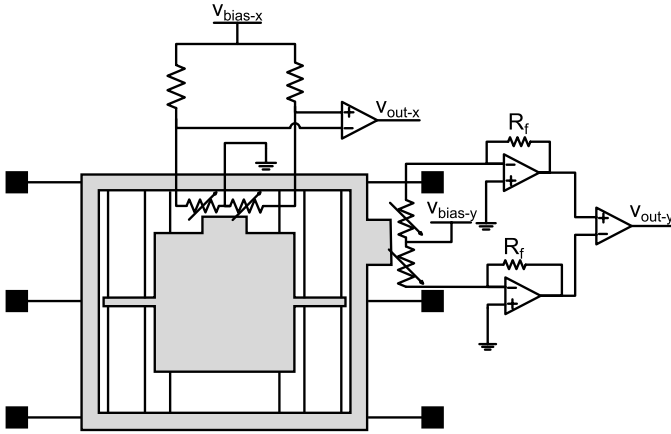


Fig. 8. Schematic diagram of the electrothermal sensors and their corresponding readout circuits.

of the outer kinematic chain drastically. The first out-of-plane mode of the system is located at approximately 6 kHz. The out-of-plane stiffness of the scan table is also obtained using FEM as 485.4 N/m.

Typically, AFM cantilevers with a bending stiffness below 10 N/m are used in contact-mode imaging [20]. In addition, the tip-sample interaction force is normally in the range of about 10 nN [20], [21], which induces an out-of-plane displacement in the scan table within the picometer range. Hence, given its high out-of-plane stiffness and resonance frequency, the scan table is expected to remain stable during imaging.

Using the force obtained from (5) in the FEM model, the displacement range expected for the device is  $\pm 7.4 \mu\text{m}$  for the X axis and  $\pm 5.2 \mu\text{m}$  for the Y axis with a maximum actuation voltage of 90 V. According to this analysis, the maximum von Mises stress in the device is approximately 140 MPa and occurs within the ‘type E’ flexures. However, this amount of stress is an order of magnitude lower than the characteristic fracture strength of about 1.97 GPa with a Weibull modulus of 8.9 for single crystal silicon [22].

#### D. Electrothermal Sensor

As mentioned in Sec. II-A, electrothermal sensors are implemented to measure the in-plane motion of the stage in each direction. As the equilibrium position of the heat sink is located halfway between the two heaters, the displacement of the heat sink creates a differential temperature variation between the heaters. The change of temperature leads to a proportional variation in their electrical resistance. For the X axis, the common electrode of the sensor is connected to the electrical ground while this electrode for the Y-axis sensor is floating.

The readout circuit used for the X-axis electrothermal sensor is the Wheatstone bridge. In Fig. 8 the schematic of the electrical connection of this circuit is shown. The variation of the resistance of the heaters due to the heat sink displacement is mapped to the output voltage of the Wheatstone bridge, and an instrumentation amplifier is used to differentially

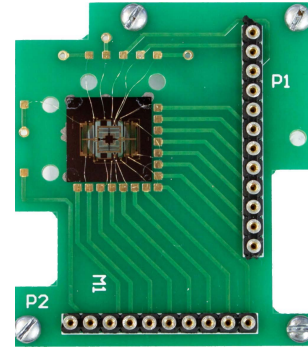


Fig. 9. MEMS die wirebonded and fixed to PCB.

amplify the output voltages. In this circuit, the bias voltage should be adjusted such that a higher sensitivity and larger voltage swing are achieved in the sensor output. However, for the X-axis electrothermal sensor, increasing the bias voltage causes the temperature of the ‘type A’ flexures in the sensor signal path to rise due to Joule heating as a consequence of the increased current flowing through them. This heat, together with fabrication imperfections in the flexures, can cause an electrothermal actuation effect within the flexures that potentially results in undesirable movement of the frame in the Y direction. Regarding this issue, a bias voltage of 12 V is experimentally adjusted for the inner stage’s electrothermal sensor.

The readout circuitry implemented for the Y-axis sensor is schematically shown in Fig. 8. This circuit consists of three sections. In the first stage, the heaters are actuated with a bias voltage. Here a voltage of 9 V, experimentally adjusted, is used as the bias voltage. In the next stage, the current passing through each heater is converted to a voltage using a V-I transimpedance circuit. Finally, the output voltages from each stage are differentially amplified using an instrumentation amplifier in the final stage.

### III. CHARACTERIZATION

For characterization, the MEMS chip was glued and wirebonded on a specially designed PCB (shown in Fig. 9). For the actuation signal routing and sensor readout circuits, another PCB was designed and mounted on a platform adjacent to the MEMS device. To obtain the static and dynamic behavior of both the scan table and the frame, a Polytec Micro System Analyzer (MSA-050-3D) was utilized. The MSA uses three laser vibrometers to measure the velocity and the displacement of the MEMS device in three dimensions. In Fig. 10, the displacement of the scan table versus the differential actuation voltage is shown for both directions. For the X and Y axes, DC biases of 50 V and 60 V were applied, respectively. The static test reveals a stroke of about  $14 \mu\text{m}$  for the X direction, and more than  $9 \mu\text{m}$  for the Y axis.

Using the linear actuation mechanism, the frequency response of the scan table for both axes was also obtained by the MSA and is illustrated in Fig. 11. As expected, the first resonant mode of the system is the in-plane mode in the Y direction located at 2.38 kHz. The second mode is

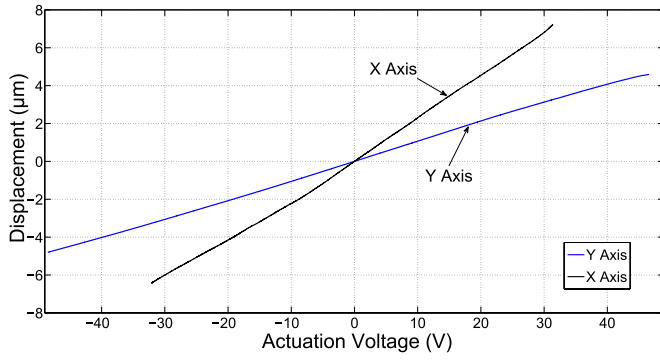


Fig. 10. Scan table static lateral displacements.

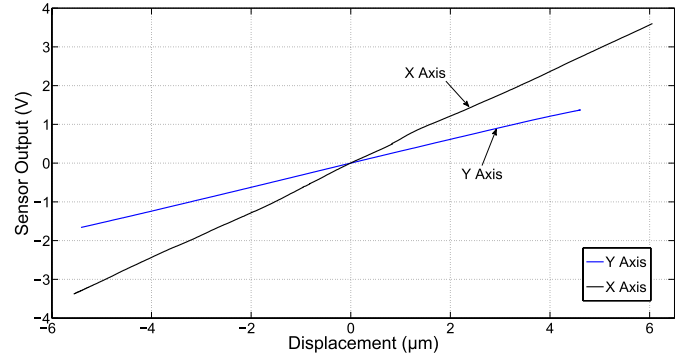


Fig. 12. The output of electrothermal sensors in both axes versus the stage displacement.

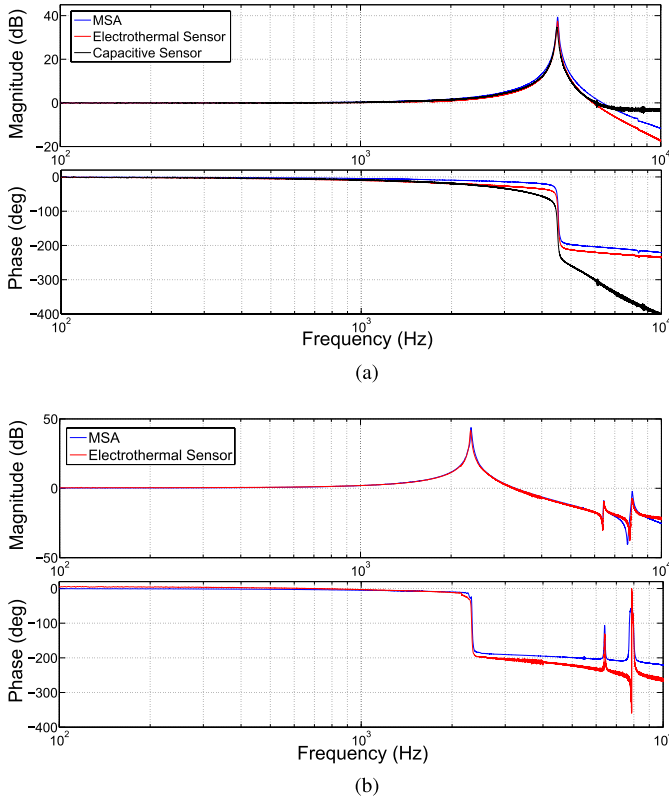


Fig. 11. Frequency response of the nanopositioner obtained by the MSA and the electrothermal sensors in both directions. (a) X-Axis. (b) Y-Axis.

the in-plane vibration mode in the X direction at 4.42 kHz. The inconsistency between the resonant mode obtained by the MSA and the FEM is most likely due to fabrication process tolerances.

During the static test, each electrothermal sensor output was also recorded separately and depicted versus the differential actuation voltage as shown in Fig. 12. It is clear that the electrothermal sensors display a linear behavior. Based on the sensor output at different actuation voltages and the stage's actual displacement as reported in Fig. 10, calibration factors of  $0.60 \text{ V}/\mu\text{m}$  and  $0.31 \text{ V}/\mu\text{m}$  are obtained for the X and Y axes, respectively.

To calculate the resolution of the electrothermal sensors, the time history of the sensor noise was recorded for both axes in

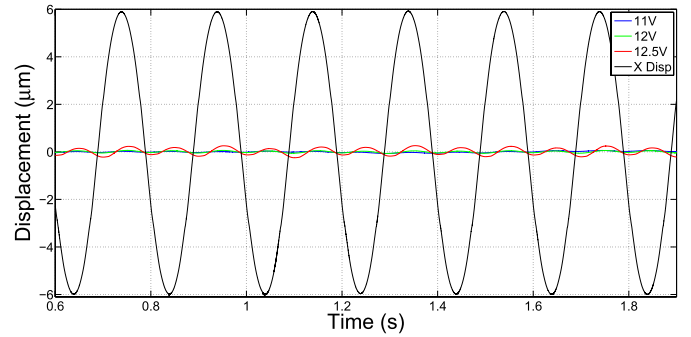


Fig. 13. Displacement of the frame in the Y direction resulting from the X direction displacement of the stage. The test was performed using a range of X-axis electrothermal sensor biases.

a bandwidth of 10 kHz. Based on the root mean square (RMS) values of the sensor noise, their resolution was determined to be 6.9 nm and 6.8 nm for the X and Y axes, respectively.

#### A. Cross-Coupling

The cross-coupling between the two axes was determined by applying a sinusoidal actuation voltage to the X axis and measuring the orthogonal movement of the frame. The cross-coupling measurement was performed in the frequency domain using the MSA, and was determined to be less than  $-60 \text{ dB}$ . Such a low cross-coupling demonstrates one of the major advantages of the serial kinematic design of the stage.

This test was performed with the nanopositioner's electrothermal sensors remaining inactive. However, as described in Sec. II-D, a segment of the electrical path for the X-axis sensor is carried over a series of flexures that permit the motion of the nanopositioner's frame in the Y direction. In order to determine if the electrothermal sensors have any effect on the nanopositioner's dynamics, an additional series of cross-coupling tests were performed where the X-axis sensors were active. The X axis was driven by a 5 Hz sinusoidal signal that produced a peak-to-peak stage displacement of approximately  $12 \mu\text{m}$ . The X-axis electrothermal sensor was initially biased with 12 V, with the resulting displacement of the Y-axis frame being measured by the MSA and shown in Fig. 13.

Based on the amplitudes of the time-domain plots shown in Fig. 13, the nanopositioner's cross-coupling in this case was

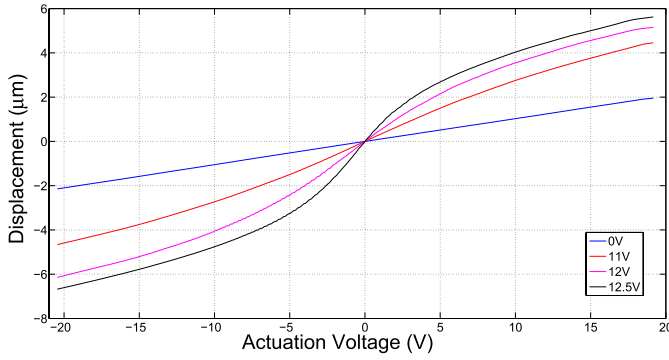


Fig. 14. The displacement in the Y axis versus actuation voltage, at different X-axis sensor biases.

calculated to be approximately  $-41$  dB. While this figure is still very low, it is nevertheless higher than the value of  $-60$  dB reported for the case where the sensors were inactive. This led to the test being repeated with two other sensor bias voltages,  $11$  V and  $12.5$  V. The results from these tests are also plotted in Fig. 13. Based on the corresponding amplitude of the Y-axis displacement, the cross-coupling between the nanopositioner's axes is calculated to be  $-49$  dB and  $-29$  dB for sensor biases of  $11$  V and  $12.5$  V, respectively.

From these results, it is clear that the bias voltage applied to the nanopositioner's X-axis electrothermal sensors does influence the behavior of the device. This effect is examined in greater detail in the following section. Additionally, these tests showed that an X-axis sensor bias of  $12$  V results in an effective compromise between the sensitivity of the sensor and the cross-coupling within the device.

#### B. Effect of Sensor Bias on Nanopositioner Behavior

Having determined that the magnitude of the cross-coupling between the nanopositioner's axes is dependent on the X-axis sensor bias, additional tests were performed to further understand this effect.

While the nanopositioner's Y-axis displacement versus applied actuation voltage was presented earlier in Fig. 10 the test was performed with the X-axis electrothermal sensors being inactive. Given the results of Sec. III-A, this test was repeated with the X-axis electrothermal sensors being biased at  $11$  V,  $12$  V, and  $12.5$  V. The displacement of the stage was recorded with the MSA and the results are shown in Fig. 14. It is evident from this figure that raising the X-axis sensor bias both increases the achievable Y-axis displacement and causes the behavior of this axis to deviate from linear. The calibration factor for the Y axis electrothermal sensor also changes slightly to approximately  $0.25\text{V}/\mu\text{m}$ , which is likely due to the electrothermal effect in the flexures.

These results suggest that the flow of current in the X-axis sensor path induces a spring-softening characteristic in the Y-axis flexure mechanism. As described in Sec. II-B, a metal electrical trace is fabricated on top of the Y-axis flexures that carry the X-axis sensor current in order to minimize the potential for Joule heating in these flexures, however imperfections in the MEMS fabrication process may nevertheless allow this effect to occur. As a result, the heating

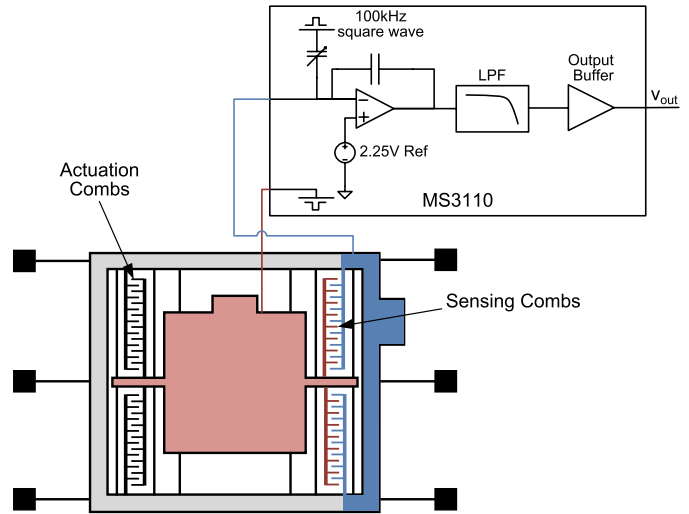


Fig. 15. Schematic diagram of MEMS nanopositioner and MS3110 capacitive readout circuit.

of these flexures may cause them to expand and thus modify the nanopositioner's Y-axis dynamics.

#### IV. CAPACITIVE SENSING IMPLEMENTATION

Despite the phenomenon described in the previous section, the X-axis electrothermal sensor functions effectively to provide real-time measurements of the displacement of the nanopositioner's inner stage. In this section, however, an alternative X-axis sensing mechanism is presented that avoids the aforementioned thermally-induced effects.

As described in Sec. II-C, the electrostatic actuators for each axis are arranged in a bidirectional configuration that allows a linear actuation mechanism to be employed. Alternatively, the actuator on one side of the stage can instead be used as part of a capacitive sensing implementation. While this does mean that the X-axis displacement range is effectively halved, the characterization of the device shows that  $7\mu\text{m}$  of motion is still achievable. This range of motion is comparable to that of many existing devices within the literature and is sufficient for various nanopositioning applications [5], [23], [24].

In this sensing implementation, the capacitance of the interdigitated combs on one side of the inner stage varies linearly with the stage's position. A number of methods may be used to convert this varying capacitance into a measurable electrical signal, including measuring shifts in the frequency of a resonant LCR circuit, however in this case a commercial Irvine Sensors MS3110 capacitive readout IC has been used simply to demonstrate the feasibility of implementing capacitive sensing for the MEMS nanopositioner. A schematic diagram of the MS3110 and its connection to the MEMS nanopositioner is shown in Fig. 15. The IC uses a charge amplifier to measure the changes in capacitance between the nanopositioner's sensing electrode and an onboard fixed capacitor. The output of the charge amplifier is passed through a low-pass filter and a buffer, resulting in an output voltage that is representative of the stage's displacement.

As the differential actuation principle can no longer be used in this configuration, a new test was performed to determine the achievable range of the X axis due to the remaining



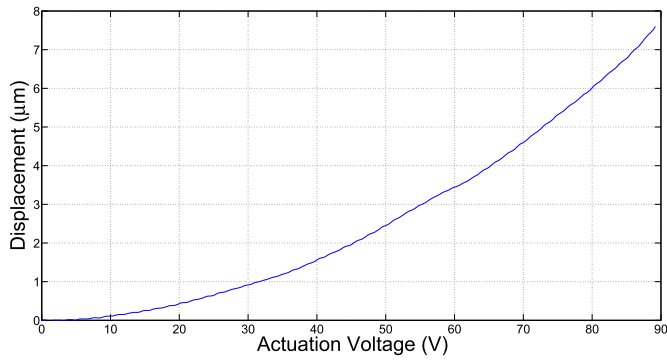


Fig. 16. Displacement of the stage in the X direction using a single-sided actuation configuration.

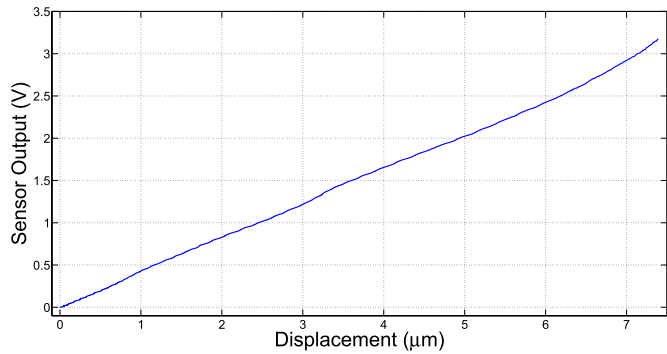


Fig. 17. The output of the MS3110 capacitive readout circuit versus the stage displacement in the X direction.

electrostatic actuator. The result is shown in Fig. 16, which indicates that over  $7\ \mu\text{m}$  can be obtained. It is noted that as the actuation mechanism is now single-sided instead of differential, the displacement-voltage characteristic becomes quadratic rather than linear.

The output of the MS3110 was simultaneously recorded, allowing the relationship between the sensor output and the stage displacement to be obtained, as shown in Fig. 17. The resulting calibration factor for the capacitive sensor is  $0.41\ \text{V}/\mu\text{m}$ .

The frequency response of the X axis was remeasured using the output of the capacitive sensor, with the result being shown in Fig. 11a together with the previous frequency responses measured using the MSA and the electrothermal sensor. It can be seen that the responses are very similar for all frequencies up to and including the axis' main resonance, showing that the capacitive sensing approach fully captures the nanopositioner's X-axis dynamics.

The positioning resolution achievable using the MS3110 was determined by measuring the RMS value of the noise in the sensor output, and was calculated to be  $7.3\ \text{nm}$ . This is comparable with the resolution obtained with the use of the electrothermal sensor.

These results demonstrate that the use of a capacitive sensing mechanism is feasible for implementation with the MEMS nanopositioner. While this method does reduce the achievable displacement of the stage in the X direction, it eliminates the nonlinear effects observed with the use of the X-axis electrothermal sensor.

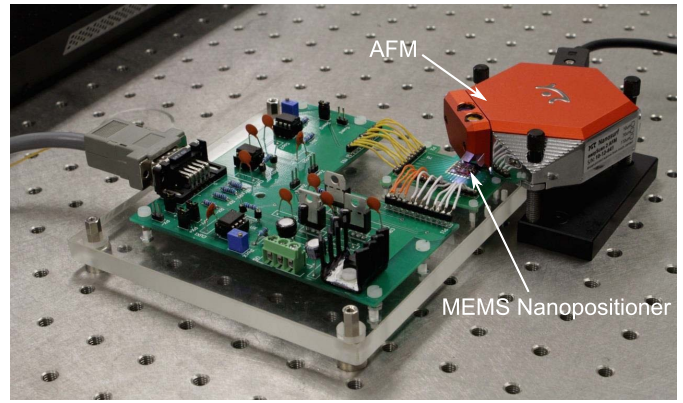


Fig. 18. Experimental setup of MEMS nanopositioner in use as the scanning stage for an AFM scan.

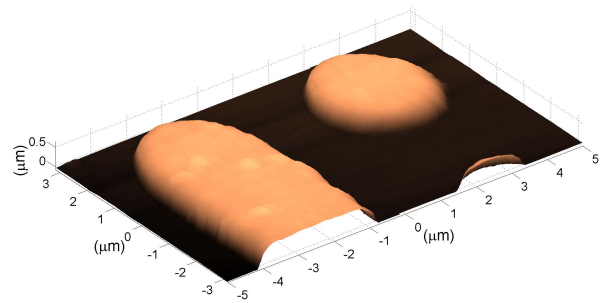


Fig. 19. AFM image of the gold features on the nanopositioner stage obtained in open-loop.

By implementing the capacitive sensing concept, it is also possible to maintain the displacement range of the stage in the X axis by using the comb drive structures simultaneously for both sensing and actuation. This is normally performed by using a high-frequency sensing signal superimposed on the actuation signal for both combs and then retrieving the displacement data using demodulation techniques [25], [26].

## V. AFM IMAGE

The nanopositioner was used as the scanning stage under a commercial Nanosurf Easyscan 2 AFM, with a photo of the experimental set-up being shown in Fig. 18. During the test, the embedded nanopositioner within the Nanosurf AFM was bypassed and the nanopositioner stage was positioned under the AFM probe. An open-loop scan was performed in constant-height contact mode. The gold features on the stage were used as the reference pattern. In Fig. 19, an AFM image of these features with  $520\ \text{nm}$  height is shown. The imaging was done using a  $6\ \mu\text{m} \times 10\ \mu\text{m}$  window size. During the scan, a triangular signal with  $4\ \text{Hz}$  frequency was applied to the X axis while the Y axis followed a slow ramp. The image was generated using the output signals of the electrothermal sensors as the in-plane position data, with the AFM cantilever deflection in the out-of-plane direction representing the features' topography.

With this imaging experiment, the capability of the device for use as a nanopositioner within an AFM is demonstrated. Various samples with micro or nanometer size such as nanotubes, viruses, bacteria, DNA, and cells can be potentially used on the scan table. Through the application of

TABLE II  
COMPARISON OF MEMS SERIAL KINEMATIC NANOPositionERS

Reference	Displacement Range ( $\mu\text{m}$ )		Resonance Frequency (kHz)		Cross-coupling	Device Size (mm)	Actuators	Sensors
	X	Y	X	Y				
Laszczyk <i>et al.</i> [13]	56	50	0.29	0.55	—	$\sim 6 \times 6$ (estimated)	Electrostatic	None
Kim <i>et al.</i> [14]	50	50	0.71	2.63	−44 dB	$7.0 \times 3.5$	Electrothermal	None
This work	14	9	4.42	2.38	−60 dB / −41 dB <sup>a</sup>	$4.80 \times 7.08$	Electrostatic	Electrothermal

<sup>a</sup> The higher cross-coupling value represents the case where the electrothermal sensors are active. Refer to Sec. III-A for details.

functionalized layers such as chitosan [27] and self-assembled monolayers [28], [29] on the scan table during a modified fabrication process, the target samples can be also immobilized on the stage for AFM imaging.

## VI. CONCLUSION

In this paper, the design and characterization of a serial kinematic MEMS electrostatic nanopositioner designed for use in an AFM were reported. By incorporating a suspended substrate method, the nanopositioner is realized through a standard SOI-MEMS fabrication technology. The fast axis achieves a high bandwidth of about 4.4 kHz. As reported in Table II, compared with the other serial kinematic MEMS nanopositioners, the proposed nanopositioner shows a higher bandwidth and superior cross-coupling rejection behavior. In addition, to allow the device to be used in an AFM, on-chip electrothermal displacement sensors are incorporated in each direction. The serial kinematic design of the stage results in extremely low cross-coupling between the lateral axes of the nanopositioner. This characteristic, combined with its high resonance bandwidth and its ability to use a feedback control loop to attain high scan speeds with high positioning precision, makes this device ideal as the scanning stage of a raster-scanned high-speed on-chip AFM.

## REFERENCES

- [1] M. A. Lantz, H. E. Rothuizen, U. Drechsler, W. Haberle, and M. Despont, "A vibration resistant nanopositioner for mobile parallel-probe storage applications," *J. Microelectromech. Syst.*, vol. 16, no. 1, pp. 130–139, Feb. 2007.
- [2] Y. K. Yong, S. O. R. Moheimani, B. J. Kenton, and K. K. Leang, "Invited review article: High-speed flexure-guided nanopositioning: Mechanical design and control issues," *Rev. Sci. Instrum.*, vol. 83, no. 12, p. 121101, Dec. 2012.
- [3] Y. Song and B. Bhushan, "Atomic force microscopy dynamic modes: Modeling and applications," *J. Phys., Condens. Matter*, vol. 20, no. 22, p. 225012, 2008.
- [4] A. G. Fowler, A. N. Laskovski, A. C. Hammond, and S. O. R. Moheimani, "A 2-DOF electrostatically actuated MEMS nanopositioner for on-chip AFM," *J. Microelectromech. Syst.*, vol. 21, no. 4, pp. 771–773, 2012.
- [5] T. Ando, "High-speed atomic force microscopy coming of age," *Nanotechnology*, vol. 23, no. 6, p. 062001, 2012.
- [6] M. W. Fairbairn and S. O. R. Moheimani, "Control techniques for increasing the scan speed and minimizing image artifacts in tapping-mode atomic force microscopy: Toward video-rate nanoscale imaging," *IEEE Control Syst.*, vol. 33, no. 6, pp. 46–67, Dec. 2013.
- [7] M. Maroufi and S. O. R. Moheimani, "Design, fabrication and characterization of a high-bandwidth 2DOF MEMS nanopositioner," in *Proc. IEEE/ASME Int. Conf. Adv. Intell. Mechatronics*, Wollongong, NSW, Australia, Jul. 2013, pp. 335–340.
- [8] A. Mohammadi, A. G. Fowler, Y. K. Yong, and S. O. R. Moheimani, "A feedback controlled MEMS nanopositioner for on-chip high-speed AFM," *J. Microelectromech. Syst.*, vol. 23, no. 3, pp. 610–619, 2014.
- [9] M. Azizi, N. Sarkar, and R. R. Mansour, "Single-chip CMOS-MEMS dual mode scanning microwave microscope," *IEEE Trans. Microw. Theory Techn.*, vol. 61, no. 12, pp. 4621–4629, Dec. 2013.
- [10] E. Guliyev *et al.*, "Quasi-monolithic integration of silicon-MEMS with piezoelectric actuators for high-speed non-contact atomic force microscopy," *Meas. Sci. Technol.*, vol. 23, no. 7, p. 074012, 2012.
- [11] M. Olfatnia, L. Cui, P. Chopra, and S. Awtar, "Large range dual-axis micro-stage driven by electrostatic comb-drive actuators," *J. Micromech. Microeng.*, vol. 23, no. 10, p. 105008, 2013.
- [12] J. Dong and P. M. Ferreira, "Electrostatically actuated cantilever with SOI-MEMS parallel kinematic XY stage," *J. Microelectromech. Syst.*, vol. 18, no. 3, pp. 641–651, 2009.
- [13] K. Laszczyk *et al.*, "A two directional electrostatic comb-drive X–Y micro-stage for MOEMS applications," *Sens. Actuators A, Phys.*, vol. 163, no. 1, pp. 255–265, 2010.
- [14] Y.-S. Kim, J.-M. Yoo, S. H. Yang, Y.-M. Choi, N. G. Dagalakis, and S. K. Gupta, "Design, fabrication and testing of a serial kinematic MEMS XY stage for multifinger manipulation," *J. Micromech. Microeng.*, vol. 22, no. 8, p. 085029, 2012.
- [15] Y. Zhu, A. Bazaei, S. O. R. Moheimani, and M. R. Yuce, "Design, modeling, and control of a micromachined nanopositioner with integrated electrothermal actuation and sensing," *J. Microelectromech. Syst.*, vol. 20, no. 3, pp. 711–719, 2011.
- [16] A. Cowen, G. Hames, D. Monk, S. Wilcenski, and B. Hardy, *SOIMUMPs Design Handbook. Revision 8.0*. Durham, NC, USA: MEMSCAP Inc., 2011.
- [17] Y. Shan and K. K. Leang, "Design and control for high-speed nanopositioning: Serial-kinematic nanopositioners and repetitive control for nanofabrication," *IEEE Control Syst.*, vol. 33, no. 6, pp. 86–105, Dec. 2013.
- [18] G. Zhou and P. Dowd, "Tilted folded-beam suspension for extending the stable travel range of comb-drive actuators," *J. Micromech. Microeng.*, vol. 13, no. 2, pp. 178–183, 2003.
- [19] R. Legtenberg, A. W. Groeneveld, and M. Elwenspoek, "Comb-drive actuators for large displacements," *J. Micromech. Microeng.*, vol. 6, no. 3, pp. 320–329, 1996.
- [20] F. J. Giessibl, "Advances in atomic force microscopy," *Rev. Modern Phys.*, vol. 75, no. 3, p. 949, Jul. 2003.
- [21] T. Junno, S. Anand, K. Deppert, L. Montelius, and L. Samuelson, "Contact mode atomic force microscopy imaging of nanometer-sized particles," *Appl. Phys. Lett.*, vol. 66, no. 24, pp. 3295–3297, 1995.
- [22] D. C. Miller, B. L. Boyce, M. T. Dugger, T. E. Buchheit, and K. Gall, "Characteristics of a commercially available silicon-on-insulator MEMS material," *Sens. Actuators A, Phys.*, vol. 138, no. 1, pp. 130–144, 2007.
- [23] N. B. Hubbard and L. L. Howell, "Design and characterization of a dual-stage, thermally actuated nanopositioner," *J. Micromech. Microeng.*, vol. 15, no. 8, pp. 1482–1493, 2005.
- [24] N. B. Hubbard, M. L. Culpepper, and L. L. Howell, "Actuators for micropositioners and nanopositioners," *Appl. Mech. Rev.*, vol. 59, no. 6, pp. 324–334, 2006.
- [25] J. Dong and P. M. Ferreira, "Simultaneous actuation and displacement sensing for electrostatic drives," *J. Micromech. Microeng.*, vol. 18, no. 3, p. 035011, 2008.
- [26] S. I. Moore and S. O. R. Moheimani, "Displacement measurement with a self-sensing MEMS electrostatic drive," *J. Microelectromech. Syst.*, vol. 23, no. 3, pp. 511–513, 2014.
- [27] B. Krajewska, "Application of chitin- and chitosan-based materials for enzyme immobilizations: A review," *Enzyme Microbial Technol.*, vol. 35, pp. 126–139, Aug. 2004.
- [28] H. Chen *et al.*, "Detection of *Saccharomyces cerevisiae* immobilized on self-assembled monolayer (SAM) of alkanethiolate using electrochemical impedance spectroscopy," *Anal. Chim. Acta*, vol. 554, pp. 52–59, Dec. 2005.
- [29] T. Wink, S. J. van Zuilen, A. Bult, and W. P. van Bennekom, "Self-assembled monolayers for biosensors," *Analyst*, vol. 122, no. 4, pp. 43R–50R, 1997.



**Mohammad Maroufi** (S'14) received the B.Sc. degree in mechanical engineering and applied physics as a Distinguished Student and the Master's degree in mechatronics from the Amirkabir University of Technology (Tehran Polytechnic), in 2008 and 2011, respectively. He is currently pursuing the Ph.D. degree in electrical engineering with the University of Newcastle, Australia. As a Visiting Researcher, he is also with the Mechanical Engineering Department, University of Texas at Dallas. His research interests

include the design and control of microelectromechanical systems (MEMS) nananopositioning systems, MEMS-based sensing and actuation, on-chip atomic force microscopy, and mechanical modeling of smart materials and structures.



**Anthony G. Fowler** (S'10–M'15) was born in Taree, NSW, Australia. He received the Bachelor's degree in electrical engineering and the Ph.D. degree in electrical engineering from the University of Newcastle, Callaghan, NSW, in 2010 and 2014, respectively, where he is currently a Postdoctoral Fellow with the School of Electrical Engineering and Computer Science. He is also a Visiting Researcher with the Department of Mechanical Engineering, University of Texas at Dallas. His research interests include the design and analysis

of novel microelectromechanical systems devices for energy harvesting and nanopositioning applications.



**S. O. Reza Moheimani** (F'11) currently holds the James von Ehr Distinguished Chair in Science and Technology with the Department of Mechanical Engineering, University of Texas at Dallas. His current research interests include ultrahigh-precision mechatronic systems, with a particular emphasis on dynamics and control at the nanometer scale, including applications of control and estimation in nanopositioning systems for high-speed scanning probe microscopy and nanomanufacturing, modeling and control of microcantilever-based devices, control

of microactuators in microelectromechanical systems, and design, modeling, and control of micromachined nanopositioners for on-chip scanning probe microscopy.

Dr. Moheimani is a Fellow of the International Federation of Automatic Control and the Institute of Physics, U.K. His research has been recognized with a number of awards, including the IFAC Nathaniel B. Nichols Medal (2014), the IFAC Mechatronic Systems Award (2013), the IEEE Control Systems Technology Award (2009), the IEEE TRANSACTIONS ON CONTROL SYSTEMS TECHNOLOGY Outstanding Paper Award (2007), and several best student paper awards at various conferences. He has served on the editorial boards of a number of journals, including the IEEE TRANSACTIONS ON MECHATRONICS, the IEEE TRANSACTIONS ON CONTROL SYSTEMS TECHNOLOGY, and *Control Engineering Practice*. He currently chairs the IFAC Technical Committee on Mechatronic Systems, and has chaired several international conferences and workshops.